Design of Supercritical Low-Reynolds Number Airfoils for Fixed-Wing Flight on Mars

Oliviu Şugar-Gabor [a, *], Andreea Koreanschi [b]

[a] *University of Salford, Salford, M5 4WT, United Kingdom ([*]Corresponding author: o.sugar-gabor@salford.ac.uk)*

[b] *University of Salford, Salford, M5 4WT, United Kingdom*

Abstract

Aerodynamic shape optimization for the high-subsonic low-Reynolds number flow regime represents an area of on-going research. The interaction between supercritical compressible flow and laminar boundary layer separation is not well understood due to the high challenges associated with setting up relevant experimental work. However, in the design of future fixed-wing aircraft for flight in extra-terrestrial atmospheres, such flow conditions might commonly occur. The present study presents a family of single-point and multi-point optimized airfoils designed for high-subsonic flight at a high-lift condition in the Martian atmosphere. A gradient-based optimizer is used, with a second-order finite-volume flow solver and a second-order continuous adjoint solver for determining surface sensitivities with respect to the objective function of minimizing drag. Both fully turbulent and transitional flow are considered, to evaluate the impact on the resulting design and to stress the importance of continuing research to develop robust shape optimization including laminar boundary layer and transition prediction. Both on-design and off-design conditions are evaluated, the airfoils obtained when considering transition effects demonstrating good overall performance.

1. Introduction

Airplanes designed for flight in the Martian atmosphere have been proposed by NASA (Braun and Spencer, 2006) and a group of Japanese researchers (Tanaka et al., 2006). Achieving fixed-wing flight in the low-density CO2-based low-temperature environment represents a very challenging problem due to the low-Reynolds number values of the order of $\mathcal{O}(10^4 - 10^5)$ and the high speeds required to produce sufficient lift. The airflow around any lifting surface in such conditions is expected to be complex, with a strong non-linear interaction between viscous and compressibility effects. Available experimental and numerical data for airfoils in the high-subsonic Mach number, low-Reynolds number flight regime is very limited in the open literature.

Anyoji et al. (2015) have investigated the aerodynamic characteristics of a NACA 0012-34 airfoil at very low Reynolds numbers of the order of $\mathcal{O}(10^4)$ and Mach numbers between 0.10 and 0.60, using a CO2-based "Mars Wind Tunnel". It was seen that the lift curve of the airfoil shows non-linear effects at low lift conditions due to the formation of laminar separation bubbles, while compressibility mainly affects high lift behaviour and stalling characteristics, however the Mach number range used did not allow for the occurrence of shock waves. Munday et al. (2015) used the same wind tunnel to conduct a study on the suitability of triangular airfoils as propeller blade sections for a Mars fixed-wing airplane concept.

Several authors have conducted numerical studies of airfoils in high-subsonic, relatively low-Reynolds number conditions, with application to High-Altitude Long-Endurance (HALE) Unmanned Aerial Vehicles (UAVs). Drela (1992) conducted an influential work on this topic. The computational study highlighted the importance of effectively using the high-Mach number flow on the airfoil's upper surface to extend laminar flow and reduce losses associated with laminar separation bubbles by increasing the transition rate in the bubble via the lambda shock. The author's remark on the lack of in-depth understanding and progress in optimal airfoil design in such flow conditions remains true even 25 year later. The Apex-16 airfoil resulted from the research presented in (Drela, 1992) was later experimentally tested as part of a very high-altitude sailplane flight, details being found in (Greer et al., 1999), but no measured flight test data was presented in the open literature.

Biber and Tilmann (2003) have performed the design of a supercritical airfoil for a HALE aircraft, using the XFOIL and MSES computational codes. The Mach numbers considered were approximately in the $0.50 - 0.70$ range, while the Reynolds number range was 0.7 to 3.0 million. It was shown that the extent of the laminar boundary layer and the behaviour of laminar separation bubbles must be accurately captured. However, such a Reynolds number range is still very high compared to what would be encountered by the Mars plane. Jung et al. (2017) designed an airfoil for flight in the Martian atmosphere using results obtained from a Reynolds-averaged Navier Stokes (RANS) flow solver and the Langtry-Menter $\gamma - Re_\theta$ transition model (Menter et al., 2004), focusing on high-subsonic flow conditions but below the critical Mach number. The lack of shock waves allowed a fully laminar flow on both upper and lower surfaces for flight on design conditions.

As part of the NASA ARES Mars airplane project, a family of cambered airfoils was designed, as reported by Smith et al. (2003). The coupled inviscid-boundary layer code MSES was used for the work, incorporating the e^N transition prediction method, and some validation was performed using a Navier-Stokes solver, with relatively good agreement between the numerical predictions. More recently (Kaynak et al., 2012), the performance of the Apex-16 airfoil has been revisited using state-of-the-art RANS-based finite volume methods and several transition prediction models including $\gamma - Re_\theta$ the $k - k_L - \omega$ model (Walters and Leylek, 2004). Comparisons were made with the MSES code results published in (Drela, 1992) and indicated significant differences in the predicted drag polar characteristics, especially at moderate-to-high C_L conditions, but no possible explanations were provided to account for these differences.

Much of the state-of-the-art aerodynamic shape optimization work is performed assuming fully turbulent flow. Even for relatively low-Reynolds number applications such as wind turbine blades, it is common to use fully turbulent RANS solvers (see for example Dhert et al., 2017), together with an adjoint method for efficiently computing the objective functional gradients, and a gradient-based optimization technique.

However, some studies involving aerodynamic shape optimization including laminar-to-turbulent transition prediction methods have been published in literature, although sparsely. The e^N method was used in a Newton-Krylov discrete-adjoint optimization framework (Driver and Zingg, 2007), in a continuous adjoint-based design methodology (Lee and Jameson, 2009), in an optimization tool based on a multi-objective genetic algorithm (Zhang et al., 2019), and in a Discontinuous Galerkin finite element framework (Halila et al., 2019). The $\gamma - Re_\theta$ model was used in a discrete adjoint-based design framework (Khayatzadeh and Nadarajah, 2011, 2014). The work of Vassberg et al. (2004) as part of the NASA ARES project must be referenced as the earliest use of RANS-based aerodynamic shape optimization in compressible flow considering transition prediction.

The research of Robitaille et al. (2015) focused on the aerodynamic shape optimization of a transonic airfoil using both fully turbulent and transitional flow approaches. Although not computationally efficient due to the use of finite-differences to estimate gradients, the work highlighted the subtle but important differences between the fully turbulent and transitional optimal shapes, as well as the need to avoid using purely Boolean (on-off type) transition correlations which can introduce oscillations in the numerical solutions and prevent steady-state convergence. Rashad and Zingg (2015) showed that robust, natural laminar flow airfoils can be obtained using state-of-the-art RANS solvers and the $\gamma - Re_\theta$ transition model, as solutions to a multi-point design optimization problem. It must be noted that these studies were all focused on high-Reynolds conditions, at both subsonic and transonic airspeeds, flow condition for which a very good understanding exists.

The present work represents (to the authors' knowledge) the first attempt to conduct a robust optimal airfoil design process for the supercritical very low Reynolds number conditions typical of the Martian atmosphere, using a state-of-the-art adjoint gradient-based optimization framework and a second-order accurate RANS finite volume flow solver including transition prediction. Section 2 briefly outlines the optimization methodology and framework, while section 3 presents the results for both single-point and multi-point optimization cases, highlighting both on and off-design performance and discussing the significant aspects observed. The work contributes to a verification and validation of state-of-the-art RANS-based aerodynamic shape optimization for low-Reynolds high-Mach number flows. In addition, an algorithm for achieving a desired lift coefficient value when the lift curve has strongly nonlinear behaviour is developed and tested, algorithm based on control-law techniques.

2. Optimization Methodology and Problem Formulation

2.1. Theoretical and Numerical Aspects

The aerodynamic shape optimization problem is solved using the SU2 open-source package (Economon, 2016). This choice is motivated by the demonstrated insensitivity of the optimal solutions obtained with the framework with respect to the optimizer setup, for transonic shape optimization scenarios (see Yang et. Al., (2018) for details). The flow around the airfoil is governed by the compressible Navier-Stokes equations, which can be expressed in differential form as:

$$\frac{\partial \boldsymbol{U}}{\partial t} + \nabla \cdot \boldsymbol{F}^c - \nabla \cdot (\mu_k \boldsymbol{F}_k^v) = 0 \tag{1}$$

Where:

$$\boldsymbol{U} = \{\rho, \rho\boldsymbol{V}, \rho E\}^T, \ \ \boldsymbol{F}^c = \{\rho\boldsymbol{V}, \rho\boldsymbol{V}\otimes\boldsymbol{V} + \bar{\boldsymbol{I}}p, \rho E\boldsymbol{V} + p\boldsymbol{V}\}^T$$

$$\boldsymbol{F}_1^v = \left\{0, \nabla\boldsymbol{V} + \nabla\boldsymbol{V}^T - \frac{2}{3}\bar{\boldsymbol{I}}\nabla\cdot\boldsymbol{V}, \left(\nabla\boldsymbol{V} + \nabla\boldsymbol{V}^T - \frac{2}{3}\bar{\boldsymbol{I}}\nabla\cdot\boldsymbol{V}\right)\cdot\boldsymbol{V}\right\}^T, \ \ \boldsymbol{F}_2^v = \{0,0,c_P\nabla T\}^T$$

In the above equations, ρ is the fluid density, $\boldsymbol{V}$ is the velocity vector, E is the total energy per unit mass, p is the static pressure, c_P is the specific heat at constant pressure, T is the temperature, $\bar{\boldsymbol{I}}$ is the unit second-order tensor, $\boldsymbol{U}$ is the vector of conservative variables, $\boldsymbol{F}^c$ and $\boldsymbol{F}_k^v$ are the convective and viscous flux vectors, and μ_k is the dynamic viscosity (when $k = 1$) or the thermal conductivity (when $k = 2$).

In the field of RANS-based aerodynamic shape optimization, using the adjoint approach for determining the gradient is very advantageous because the computational cost of computing the derivatives in a gradient is practically independent of the number of design variables. A functional of interest $J(S)$ for an aerodynamic shape optimization problem is dependent on the shape of the boundary S and the variables $\boldsymbol{U}$ describing the flow state. The total derivative of J is given by:

$$\frac{dJ}{dS} = \frac{\partial J}{\partial S} + \frac{\partial J}{\partial \boldsymbol{U}}\frac{d\boldsymbol{U}}{dS} \tag{2}$$

Evaluating the changes in the flow variables with respect to changes in boundary shape requires an additional flow solution for each geometry modification, being an extremely computationally expensive procedure. However, the total derivative of the flow solution with respect to boundary shape changes can be obtained by observing that the total derivative of the flow equations $\boldsymbol{R}(S, \boldsymbol{U})$ with respect to S vanishes for a feasible steady-state solution:

$$\frac{d\boldsymbol{R}}{dS} = \frac{\partial \boldsymbol{R}}{\partial S} + \frac{\partial \boldsymbol{R}}{\partial \boldsymbol{U}}\frac{d\boldsymbol{U}}{dS} = 0 \tag{3}$$

The above expression provides a linear system whose solution is the total derivative of the flow solution with respect to changes in the geometry shape:

$$\frac{d\boldsymbol{U}}{dS} = -\left[\frac{\partial \boldsymbol{R}}{\partial \boldsymbol{U}}\right]^{-1}\frac{\partial \boldsymbol{R}}{\partial S} \tag{4}$$

Substituting the solution of this linear system into Equation (2) gives:

$$\frac{dJ}{dS} = \frac{\partial J}{\partial S} + \frac{\partial J}{\partial \boldsymbol{U}}\left[\frac{\partial \boldsymbol{R}}{\partial \boldsymbol{U}}\right]^{-1}\frac{\partial \boldsymbol{R}}{\partial S} \tag{5}$$

The adjoint equation is set up as:

$$\left[\frac{\partial \boldsymbol{R}}{\partial \boldsymbol{U}}\right]^{T}\boldsymbol{\Psi} = -\left[\frac{\partial J}{\partial \boldsymbol{U}}\right]^{T} \tag{6}$$

Where $\boldsymbol{\Psi}$ are the adjoint variables. In the adjoint equation, the boundary shape changes do not appear explicitly, and thus the adjoint solution does not depend on the design variables introduced to create those boundary shape changes. This constitutes the major advantage of the adjoint method: the cost of obtaining the adjoint variables is independent of aspects related to geometry parameterization and the number of design variables.

Once the adjoint solution is obtained, it is substituted into the total derivative of the objective functional, giving:

$$\frac{dJ}{dS} = \frac{\partial J}{\partial S} + \frac{\partial J}{\partial \boldsymbol{U}}\boldsymbol{\Psi}^{T}\frac{\partial \boldsymbol{R}}{\partial S} \tag{7}$$

The equations presented above represent a conceptual description of the adjoint method. Within the SU2 solver, the continuous-adjoint approach is used, where Equation (6) is a partial differential equation. The calculation of the objective functional $J(S)$ gradient with respect to variations in the shape of the boundary S is achieved by solving the following continuous-adjoint RANS equations:

$$-\frac{\partial \boldsymbol{\Psi}^T}{\partial t} - \nabla \boldsymbol{\Psi}^T \cdot (\boldsymbol{A}^c - \mu_k \boldsymbol{A}_k^v) - \nabla \cdot (\nabla \boldsymbol{\Psi}^T \cdot \mu_k \overline{\boldsymbol{D}}_k^v) = 0 \tag{8}$$

The various Jacobian matrices $\boldsymbol{A}^c$, $\boldsymbol{A}_k^v$, $\overline{\boldsymbol{D}}_k^v$ obtained from the linearization of the governing equations can be found in the work of Bueno-Orovio et al. (2012) and were omitted here for reasons of brevity.

After satisfying the adjoint system indicated above, the final expression for the objective functional variation becomes:

$$\delta J(S) = \int_S \left[\boldsymbol{n} \cdot \mu_1 \left(\nabla \boldsymbol{\varphi} + \nabla \boldsymbol{\varphi}^T - \frac{2}{3} \overline{\boldsymbol{I}} \nabla \cdot \boldsymbol{\varphi}\right) \partial_n \boldsymbol{V} - \mu_2 c_P \nabla_S \Psi_5 \cdot \nabla_S T\right] \delta S d\Sigma \tag{9}$$

Where $\boldsymbol{n}$ is the outward-pointing unit vector, $\boldsymbol{\varphi}$ is the adjoint velocity vector and $\nabla_S(\,) = \nabla(\,) - \partial_n(\,) \cdot \boldsymbol{n}$ is the tangential gradient operator at the surface S. This equation provides the surface sensitivity, a measure of the variation of the objective functional with respect to variations of the boundary shape.

Laminar-to-turbulent transition location was determined using the correlation-based algebraic transition model recently developed by Cakmakcioglu et al. (2018) (referred to as the BC model). The underlying turbulence model is the well-known Spalart-Allmaras model (Spalart and Allmaras, 1992), in which the production term is multiplied with an intermittency function γ_{BC}:

$$\frac{\partial \tilde{\upsilon}}{\partial t} + u_j \frac{\partial \tilde{\upsilon}}{\partial x_j} = \gamma_{BC} c_{b1} \tilde{S} \tilde{\upsilon} - c_{w1} f_w \left(\frac{\tilde{\upsilon}}{d}\right)^2 + \frac{1}{\sigma}\left\{\frac{\partial}{\partial x_j}\left[(\upsilon + \tilde{\upsilon}) \frac{\partial \tilde{\upsilon}}{\partial x_j}\right] + c_{b2} \frac{\partial \tilde{\upsilon}}{\partial x_j} \frac{\partial \tilde{\upsilon}}{\partial x_j}\right\} \tag{10}$$

The intermittency function is defined as:

$$\gamma_{BC} = 1 - exp\left(-\sqrt{A_1} - \sqrt{A_2}\right) \tag{11}$$

Where:

$$A_1 = \frac{max\left(Re_\theta - Re_{\theta_C}, 0.0\right)}{\chi_1 Re_{\theta_C}}, \quad A_2 = \frac{max(\upsilon_{BC} - \chi_2, 0.0)}{\chi_2}$$

$$Re_\theta = \frac{Re_v}{2.193}, \ \ Re_v = \frac{\rho d^2}{\mu}\Omega, \ \ Re_{\theta_C} = 803.73(Tu_\infty + 0.6067)^{-1.027}$$

$$\upsilon_{BC} = \frac{\upsilon_t}{Ud}, \ \ \chi_1 = 0.002, \ \ \chi_2 = 5.0$$

In the above, ρ is the local density, d is the distance to the nearest wall, Ω is the vorticity, μ is the local dynamic viscosity, Re_v is the vorticity Reynolds number, Re_{θ_C} is the transition onset critical momentum thickness Reynolds number, Tu_∞ is the freestream turbulence intensity in percentage, υ_t is the kinematic turbulent viscosity, U is the local velocity magnitude and Re_∞ is the freestream Reynolds number. It must be noted that the BC model is not Galilean invariant due to the presence of the local velocity magnitude in υ_{BC}, while the χ_2 term introduces a dependency on an arbitrary reference length through Re_∞. Validation cases for compressible high-Reynolds flows have been presented in (Cakmakcioglu et al., 2018) and (Kaynak et al., 2019). To increase the level of confidence in the BC transition model, additional validation cases are presented in the paper, focusing on low-Reynolds number flows.

The Navier-Stokes equations (1) and the adjoint equations (8) are recast in integral form and discretised using a finite-volume method on a dual grid, the control volumes being constructed using a median-dual vertex-based scheme (Economon et al., 2016). The convective numerical fluxes for both direct and adjoint flow equations are evaluated using the second-order accurate Jameson-Schmidt-Turkel (JST) scheme (Jameson et al., 1981), gradients are calculated using a least-squares approach, while time-marching to steady-state is achieved using an implicit Euler method. The solution of the linearized equations is done using the Generalized Minimal Residual (GMRES) method, and convergence acceleration is achieved by a 3-level V-cycle agglomeration multigrid strategy, for both direct and adjoint equations (Economon et al., 2016). The turbulence model equation and the adjoint turbulence equation are solved segregated, using a second-order upwind scheme.

2.2. Geometry Parameterization, C_L Control Method and Optimization Problem

For parameterizing the geometry, the Free-Form Deformation (FFD) method (Sederberg and Parry, 1986) is used, initially developed for computer graphics applications. The baseline geometry is initially embedded in a B-spline control volume. The coordinates are mapped with respect to a set of control points on the box outer boundary. Modifications made on the external surface of this box then implicitly affect the object inside the volume. The design variables of the shape optimization problem are represented by the coordinates of the control points on the box boundary. To keep a feasible design space, the motion of these points with respect to their initial position can be easily constrained in terms of both permitted direction of motion and maximum displacement. This approach is particularly compact and efficient because it does not parametrize the shape itself but rather its deformation, thus also facilitating geometry sensitivity calculations. Additionally, it allows for enough flexibility to parameterize even non-conventional geometries (He et al., 2019), expanding the possible design space.

The SciPy implementation of the Sequential Least Squares Programming (SLSQP) gradient-based constrained optimization algorithm (Kraft, 1988) is used to determine the optimal airfoil shapes, the optimization variables being the FFD box control points coordinates.

Due to the expected non-linearity of the lift curve (see (Anyoji et al., 2015) for details), a method inspired from control theory was implemented in the SU2 package to maintain C_L at a desired value. Letting $e = C_L^{ref} - C_L$ be the error between the reference and current lift coefficient values, the airfoil angle of attack adjustment is done using the following Proportional-Integral-Derivative (PID) control law inspired approach:

$$\Delta\alpha = K_p e + K_d[e(n) - e(n-1)] + K_i \sum_{0}^{n} e(n) \tag{12}$$

Where K_p, K_d and K_i are the gains and n represents the current iteration number. The angle of attack correction is calculated at all iterations, in order to update the discrete-integral term, but it is actively applied only a few numbers of times during the iterative process of marching to steady-state conditions. The gains have to be manually adjusted depending on the problem, with the values used for the present work being $K_p = 0.05$, $K_d = 0.005$ and $K_i = 0.005$. These values have been found to minimize $C_L^{ref} - C_L$ is as little iterations as possible for the particular problem investigated here.

The Apex-16 airfoil designed by Drela (1992) is used a baseline geometry, embedded in an FFD box having 21×2 (chordwise and vertical) equally-spaced control points, for a total of 42 design variables. These points are constrained to displace only vertically, with the maximum displacement limited to $0.10c$. To avoid non-physical shapes resulting from the intersection of the airfoil upper and lower surfaces, constraints are introduced by enforcing positive thickness ($y_{upper} > y_{lower}$) at all x-coordinates. In addition, the maximum thickness of the optimized airfoil is required to be greater than $0.10c$. The objective is to minimize the drag coefficient subject to the specified geometric constraints and can be written as:

$$\min_{\boldsymbol{P}} \sum_{k=1}^{N_f} w_k \, C_D\left(\boldsymbol{P}, C_L^{ref}, M_k, Re_k\right) \qquad (13)$$

$$subject\ to\ g_i(\boldsymbol{P}) \leq 0$$

Where $\boldsymbol{P}$ is the vector of design variables (coordinates of FFD box control points), M_k, Re_k are the Mach and Reynolds number defining the flight condition, $w_k \leq 1$ are user-defined weights and $g_i(\boldsymbol{P})$ represent the geometric constraints.

This formulation permits an optimization for both single-point and multi-point cases (if the number of flight conditions $N_f > 1$). It must be noted that the constant lift coefficient constraint is enforced directly in the flow solver through the PID-type technique rather than being included in the optimization problem list of constraints. This approach permits achieving some savings in the total computational time, as an adjoint problem for C_L functional no longer needs to be solved.

2.3. Grid Convergence Study

A grid convergence study was done to determine the required resolution. A sequence of three C-type grids was generated using a refinement ratio of 2, grids whose properties are summarised in Table 1.

The convergence study was done at a Mach number of 0.68, a Reynolds number of 2.26×10^5 and an angle of attack of 2°.Both fully turbulent and transitional cases were analysed, the results being presented in Table 2.

Figure 1 plots the convergence behaviour for better visualization, where C_0 represents the Richardson extrapolation of the coefficient and N is the number of cells. As can be seen from both this and Table 2, the range of convergence is close to one for all coefficients, indicating the solutions are in the asymptotic range of convergence. As expected, the transition model requires a more refined grid compared to a fully turbulent solution under the same conditions to achieve grid-independent drag coefficient values. Rather surprisingly, the C_L and C_m orders of convergence are better when transition is considered. Figure 2 plots a typical convergence history for the density residual and drag coefficient. The solution obtained with the SA-BC model requires slightly more iterations until steady coefficient values are obtained, however the residual decrease for the high iteration number range is relatively unchanged. Following the convergence study, it was decided to use the fine level grid for the shape optimization work. A close-up view of the grid in the vicinity of the airfoil surface can be seen in Figure 3.

The impact of the PID-type C_L control method on the convergence behaviour is shown in Figure 4. The airfoil is set at a Mach number of 0.68, a Reynolds number of 2.26×10^5 and an initial angle of attack of 2°, with a desired $C_L^{ref} = 0.80$. The angle of attack correction is applied every 5000 iterations. Both turbulent and transitional solutions achieve a density residual drop of 6 orders of magnitude in 30000 iterations, with some visible differences in the C_L convergence history.

2.4. Validation Studies

A study was performed to verify the capabilities of the BC transition model for high-Mach low-Reynolds number flow. Experimental results matching the flight conditions considered in this paper were not found in literature. However, the work of Anyoji et al. (2015) includes wind tunnel results for a NACA 0012-34 airfoil at a very low Reynolds numbers of 1.1×10^4 and a subcritical Mach number of 0.61, using CO2 as the working fluid. These experimental results were obtained as part of a study aimed at understanding airfoil aerodynamics in the Martian atmosphere and are considered to be a suitably challenging verification case, even if the flight conditions are not matching. The solver was set up as indicated in section 2.1, while the grid properties are similar to the fine level grid generated for the convergence study.

Figure 5 presents a comparison between the numerical and experimental drag polar (left) and lift curve (right). It can be observed the numerical results obtained with the BC model capture the non-linearity of the lift curve, but the high angle of attack behaviour is not well captured, with much higher predictions of $C_{L_{max}}$ and stalling angle. The drag estimation is good up to $C_L \cong 0.55$. It must be noted that no information was provided in [3] about the turbulence intensity level in the wind tunnel, the value being arbitrarily set to 0.05% in the numerical setup. Equally important is the fact that for the high angles of attack range, the solver did not obtain steady-state convergence. The unsteady behaviour did not show any periodicity to allow for a clear selection of an averaging interval. To better isolate the average values, the random variations of coefficient values in the results are first filtered out using a moving average build with quadratic regression over intervals of 50 iterations, and then the filtered data is averaged over 40,000 iterations to output the coefficient value. Although this procedure is questionable, [3] does not specify whether the flow was naturally unsteady during the experimental test, and if so, how the average coefficient values were determined. The behaviour in the numerical results is attributed to solver capturing flow unsteadiness in the separated region, though noting again that boundary layer separation prediction is not accurate.

A second validation case was done using the experimental work of McGhee et al. (1988) on the Eppler E387 airfoil. The tests were conducted in the low-turbulence pressurised tunnel at Langley Research Centre. The case chosen is for a Reynolds number of 2.00×10^5, similar to the value used for the optimization cases, while the Mach number is only 0.06. This verifies the capabilities of the BC transition model for low-Mach low-Reynolds number flow. The freestream turbulence intensity estimated during the experimental tests was 0.05%, value also used for the numerical results. Again, the solver setup follows the details presented in section 2.1, with a grid similar to the fine level grid generated for the convergence study.

The comparison between the numerical and experimental drag polar and lift curve is shown in Figure 6. There is generally a very good agreement in terms of both lift and drag coefficient values, especially for the mid to high C_L. The numerically predicted maximum lift coefficient and stalling angle are slightly higher than the observed values, however the difficulties of RANS-based turbulence models to accurately predict trailing-edge boundary layer separation are well documented. There numerically predicted C_D values at the low C_L conditions are too high, however (McGhee et al., 1988) does not include skin friction measurements to verify whether the behaviour is caused by early laminar-to-turbulent transition by the BC model.

3. Results and Discussion

3.1. Preliminary Aspects

In evaluating airfoil performance characteristics, the so-called reduced Mach and Reynolds numbers (Drela, 1992) represent very useful parameters, as they remain unchanged as an aircraft undergoes trim changes. However, calculating representative values requires knowledge about the aircraft weight, wing loading and wing aspect ratio. Since these values have yet to be fixed in the present study, it was decided to work with the true Mach and Reynolds number values.

The Martian atmosphere is 95% CO2, 2.7% N2 and 2.3% other gases, with a mean surface atmospheric temperature of 214K, mean pressure of 640 Pa and mean density of 0.0155 kg/m3 (Young, 2000). Although these parameters vary significantly spatially and temporally, the values indicated are considered sufficiently accurate for the purpose of designing an airfoil for low-altitude flight in the equatorial region. The Mach number range considered is $0.66 - 0.70$, which leads to a Reynolds number range of $2.19 - 2.33 \times 10^5$, for a constant, unit airfoil chord. It is assumed the gas mixture behaves as a perfect gas, having a ratio of specific heats of $\gamma = 1.289$ and a specific gas constant of $R = 189\, J/(Kg \cdot K)$.

The reference molecular viscosity of the Martian atmosphere is $1.289 \times 10^{-5}\ kg/(m \cdot s)$ (Young, 2000). The dynamic viscosity as function of temperature is obtained using Sutherland's law:

$$\mu = \mu_0 \left(\frac{T}{T_0}\right)^{3/2} \frac{T_0 + S}{T + S} \tag{14}$$

Where $\mu_0 = 1.289 \times 10^{-5}\ kg/(m \cdot s)$, $T_0 = 214\ K$ and $S = 270\ K$, with the constants taking values representative for the CO2-based atmosphere.

There is no data available for average turbulence intensity levels at low altitudes in the Martian atmosphere. Assuming calm meteorological conditions, it was assumed these levels would be similar to those at relatively high altitudes in Earth's atmosphere, assuming still air, for which measurements exist (Riedel and Sitzmann, 1998). Thus, the freestream turbulence intensity considered is 0.04%.

3.2. Optimization Results and On-Design Performance

To better understand the impact of the laminar boundary layer on the airfoil optimal shapes, the optimization was done in both transitional and fully turbulent modes, with the objective of minimizing the drag coefficient and subject to the geometry constraints presented earlier. The multi-point case includes three flight conditions, at $M = 0.66, 0.68\ and\ 0.70$, with equal weights $w_k = 0.3333$. For all optimization runs the lift coefficient is fixed at the relatively high value of $C_L^{ref} = 0.80$, in order to provide sufficient lift force under low dynamic pressure conditions. The angle of attack is a free variable which can be adjusted accordingly by the solver during the optimization runs.

A summary of the optimization process results is presented in Table 3. As expected, the single-point optimized airfoils outperform the multi-point airfoil at their respective Mach numbers. It interesting to note that for $M = 0.70$, the drag obtained with the transition model is higher than the fully turbulent drag, behaviour attributed to laminar boundary layer separation which was corrected but not fully alleviated during the single-point optimization scenario. Except for the highest Mach number case, the drag difference between multi-point and single-point optimized airfoils is lower in the transitional case, indicating that multi-point designs could achieve good overall performance in such flight conditions.

Figures 7 and 8 show the outline of the multi-point and three single-point optimal airfoils obtained for transitional and fully turbulent conditions. Similarities can be observed in the shape of the single-point designs at Mach 0.66 and 0.68 for both models, the airfoils showing a relatively flat lower surface for the first $0.50c$, a maximum thickness location towards mid-chord, as well as a continuously curving upper surface (unlike classical high-Reynolds number supercritical airfoils). The multi-point airfoils show a higher leading-edge radius, higher maximum thickness and an unusual concave lower surface for approximately $0.20c$ from the leading edge, especially visible for the transitional airfoil. These features contribute to increasing the generated C_L at lower angle of attack values without requiring too high camber, point which is also corroborated by the lower angle of attack required to generate $C_L^{ref} = 0.80$ compared to the single-point designs.

The transitional $M = 0.70$ airfoil is closer in shape to the multi-point design, but with a rear shift in maximum camber location, which is translated into a more favourable pressure gradient for extending laminar flow and avoiding upper surface shocks. The differences observed between the transitional and turbulent airfoil shapes is a very strong argument for the need of robust aerodynamic shape optimization including transition prediction for any low-Reynolds design cases.

Figures 9 and 11 present the pressure coefficient distribution for the multi-point and single point airfoils at the three design conditions, while Figures 10 and 12 show the variation of the skin friction coefficient. There are important differences in the pressure variation between the transitional and fully turbulent cases, most notably the shock located before $0.30c$ at all Mach numbers for the latter, as seen in Figure 11. The transitional single-point airfoils show a pressure plateau up to $0.60c$, followed by an isentropic recompression, while the multi-point airfoil develops a weak shock at approximately $0.40c$ for all Mach numbers considered. The leading-edge pressure peak seen in the fully turbulent results is absent from the transitional airfoils pressure distribution, leading to local flow conditions more favourable for a laminar boundary layer. There is also an increase in the contribution to lift generation from the lower surface, compared to the multi-point airfoil, as seen from the more positive lower surface pressure curves in Figure 9. The skin friction curves presented in Figure 10 indicate that the single-point optimized airfoils achieve a greater extent of laminar flow on the upper surface, as expected due to the pressure plateau, the delay in pressure recovery and the weaker adverse pressure gradient. The results for $M = 0.70$ show laminar boundary layer separation and the formation of a reverse-flow region for both single-point and multi-point airfoils, as indicated by the negative C_F values on the aft part of the chord, thus justifying the relatively poor performance which was mentioned earlier.

It is worth noting that laminar separation bubbles are present at $M = 0.66$ and $M = 0.68$, followed by flow reattachment. The flow reattachment (and thus avoiding bubble bursting and significant flow separation) is possible due to a less-severe adverse pressure gradient compared to that caused by a stronger upper surface shock wave. The single point $M = 0.68$ airfoil experiences laminar separation, however its overall drag coefficient is still lower compared to the multi-point design due to a more favourable pressure distribution up to $0.60c$. As expected, the fully turbulent results of Figure 12 reveal a simpler behaviour, with generally less difference between the multi-point and single-point airfoils, and with turbulent separation on the upper surface aft of $0.80c$ at all three Mach number values.

Figures 13 and 14 present a comparison of the Mach number contours between both transitional and turbulent multi-point and single-point optimized airfoils for a freestream Mach number of 0.68. The variations in the Mach number directly relate with the comments previously made using the pressure coefficient distributions. The turbulent airfoils show a pocket of supersonic flow located on the upper leading-edge region, the multi-point transitional foil shows a rearward shift in the location of the supersonic pocket, while the single-point foil achieves a smoother isentropic airflow over the upper surface.

A breakdown of the pressure C_{D_p} and friction C_{D_f} drag components for the airfoil obtained following the optimization process is presented in Table 4. The values indicate the drag reduction achieved by the single-point designs is generally balanced between pressure (including wave drag reductions from weaker upper surface shocks) and friction drag components (attributed to an extended laminar region in the transitional case and changes in pressure gradient magnitude and local flow velocities in the fully turbulent case).

3.3. Off-Design Performance

The off-design performance of each optimized airfoil is investigated by conducting a Mach ramp study, in order to capture the drag-divergence behaviour. The lift coefficient is fixed at $C_L^{ref} = 0.80$, while the Mach number is varied between 0.60 and 0.76. The drag rise curves are shown in Figure 15. With the exception of the $M = 0.70$ single-point airfoil, the other three airfoils have relatively similar off-design performance in the transitional case, showing a small, gradual C_D increase up to $M = 0.68$, after which the drag significantly rises. This shows the airfoils are suitable for operating in a Mach number range larger than the design condition without suffering severe performance losses. In fully turbulent flow, the difference between the drag rise curves is more pronounced, each airfoil experiencing significant drag rise for freestream Mach number higher than the design condition. This behaviour is attributed to the presence of the stronger shock wave near the leading edge and the higher wave drag component.

Figures 16 and 17 present the Mach contours around the transitional and fully turbulent $M = 0.66$ single-point optimal airfoils, when operating on-design (left picture) and off-design at $M = 0.73$ (right picture). On-design, both airfoils show a shock-free flow field, which can also be correlated with the pressure distributions shown in the left-hand image of Figures 9 and 11. Off-design, the transitional foil experiences massive shock-induced boundary layer separation, the shock being located at approximately $0.40c$. The fully turbulent airfoil develops a stronger shock (thus higher wave drag) located further downstream, but the impact on the turbulent boundary layer is less significant.

The drag polar of the designed airfoils is depicted is Figure 18 for the transitional flow case and Figure 20 for the fully turbulent flow, while the lift curves are shown in Figures 19 (transitional) and 21 (turbulent). Each polar was constructed at the Mach number for which the single-point airfoils were optimized, with the multi-point foil being analysed at all three Mach number values.

In the transitional case, the single-point optimized designs tend to consistently outperform the multi-point airfoil for C_L values at and above the design value of 0.80. The delay in stall is due to a more favourable interaction between the laminar boundary layer separation and the isentropic upper surface flow. The lift curves shown in Figure 19 indicate the multi-point foil generates more lift at a given angle of attack, as was expected based on the lower surface curvature. However, it stalls earlier and achieves a lower $C_{L_{max}}$ value for all three Mach numbers. It is also interesting to note the nonlinear nature of the lift curve observed at $M = 0.70$, attributed to the laminar separation on the upper surface (behaviour also indicated in Figure 10). In the fully turbulent case, there is much less variation in the aerodynamic characteristics between single-point and multi-point designs. At both $M = 0.66$ and $M = 0.68$, the single-point airfoil achieves lower drag over almost the entire range of angles of attack. This behaviour is attributed to a lower wave drag achieved by a weaker upper surface shock not only for the design C_L, but over a more significant lift coefficient range. Again, a decrease in the generated lift at a given angle of attack can be seen in Figure 21, but much lower compared to the transitional case. The loss in lift could be overcome by setting more tighter bounds on the angle of attack variation during the optimization process.

With relatively mature computational methods such as those chosen for this work, some degree of confidence can be achieved with respect to the obtained airfoil designs, but much more work is required with respect to experimental verification and validation. This is however an extremely challenging task. Wind tunnels capable of replicating the atmospheric conditions on Mars are very rare in laboratories throughout the world, and only one, used in the work of Anyoji et al. (2015) can achieve airspeeds in the compressible regime. Mach and Reynolds similarity to flight on Mars by very-high altitude flight on Earth is equally challenging, requiring models smaller than the Mars airplane flying at altitudes preferably above 30,000 m. Significantly more work is required before the challenges introduced by the high-speed flight of a fixed-wing Mars airplane are fully understood.

4. Conclusions

The paper presents the robust design of multi-point and single point airfoils suitable for flight in the challenging high-Mach low-Reynolds number regime as would be encountered in the Martian atmosphere. The aerodynamic shape optimization was done using a gradient-based optimizer and the state-of-the-art SU2 flow solver. Three Mach numbers were considered, and a relatively high lift coefficient required due to the low dynamic pressure. The optimization was performed using both transitional and fully turbulent models, in order to highlight the differences in optimal design shape. The results have shown:

1) There are non-negligible differences in the airfoil shapes between transitional and fully turbulent flow. Although aerodynamic shape optimization including laminar to turbulent transition is not very widely used, it can be used to obtain robust designs for more challenging flight conditions, such as extra-terrestrial flight or very high-altitude transonic aircraft.

2) The transitional multi-point airfoil achieves very good performance at $M = 0.66$ and $M = 0.68$, with only small drag penalty compared to the single-point designs but is not efficient at $M = 0.70$ due to massive laminar boundary layer separation.

3) An isentropic laminar upper surface flow can be achieved with adequate airfoil design, showing more favourable high-lift behaviour and increased $C_{L_{max}}$ without incurring significant penalties at higher Mach number off-design conditions, and achieving good performance at lower-than-design Mach numbers.

4) The success of high-Mach low-Reynolds high-lift airfoil designs hinges on using the high-speed flow on the upper surface to extend laminar flow as much as possible and avoid laminar flow separation due to a strong shock generated at laminar separation bubbles, leading to bubble bursting and significant flow separation.

Data Availability

Some or all data, models, or files generated or used during the study are available from the corresponding author by request. These include generated grid files, solver configuration files, solver source code files modified compared to SU2 repository and selected results files.

Appendix

It can be observed (Figures 9 and 11) that the shock on the upper surface of the airfoils does not appear to be captured as well as would be normally expected in a grid-independent solution. To improve the quality of shock capturing, more refined grids were created and tested, as well as reduced artificial dissipation coefficients in the JST scheme. However, the changes observed with respect to shock capturing remained minimal.

Methods for analytically investigating the inner structure of a normal shock wave have been proposed in literature (for example Puckett and Stewart (1950) or Cohen and Moraff (1971)). An analysis derived from that of Puckett and Stewart (1950) is used to understand if any differences exist in the shock structure and thickness due to the different environment on Mars.

Assuming one-dimensional flow of a perfect gas having constant specific heat at constant pressure, the following ordinary differential equation (ODE) can be deduced for the smooth variation of the velocity across the shock wave:

$$\frac{du}{dx} = \left(\frac{H - \frac{u^2}{2}}{H - \frac{u_1^2}{2}}\right)^{-0.75} \frac{\sigma}{\mu_1}\left[\rho_1 u_1 \frac{\gamma + 1}{2\gamma} + \rho_1 u_1 \frac{H\frac{\gamma - 1}{\gamma}}{u} - (\rho_1 u_1^2 + p_1)\right] \tag{A1}$$

The conditions upstream of the shock are denoted with a 1-subscript, these being the velocity u_1, density ρ_1, pressure p_1 and dynamic viscosity μ_1. The other parameters are the Prandtl number σ and the ratio of specific heats γ. The flow is assumed adiabatic, so the total enthalpy H remains constant.

Solving this ODE using finite differences until the velocity becomes constant and equal to the velocity downstream of the shock, an estimate of the shock thickness can be obtained.

The normal shock thickness was calculated both for flow conditions typical of the Martian atmosphere (as defined in section 3.1 of the paper), and flow in the Earth atmosphere at an altitude of 11,000 m. This 11km condition was chosen as a comparison case due to its high occurrence in research dealing with supercritical flow over airfoils. A plot of the ratio between normal shock wave thickness on Mars and on Earth as function of the upstream Mach number is depicted in Figure A1 below.

Interestingly, it can be seen that the thickness ratio is around 2 at an upstream Mach number of 1.05, rapidly increases to 20 at a Mach number of 1.3 and then asymptotically tends to a value of around 23. For many of the optimisation cases analysed in this research, the Mach number upstream of the shock is slightly higher than 1.2, meaning that shocks appearing on the airfoil's upper surface would be 16-17 times thicker compared to flight at a typical 11km in Earth's atmosphere.

It is unclear at this moment if this analysis can provide the explanation of the relatively low quality of the shock capturing observed in the CFD results, or at least a part of the explanation. More research is needed aimed at investigating the performance of shock-capturing schemes in such extreme flow conditions.

References

Anyoji, M., Numata, D., Nagai, H. and Asai, K. (2015) Effects of Mach Number and Specific Heat Ratio on Low-Reynolds-Number Airfoil Flows, AIAA Journal, vol. 53, no. 6, pp. 1640-1654.

Biber, K. and Tilmann, C. P. (2003) Supercritical Airfoil Design for Future HALE Concepts, 41st Aerospace Sciences Meeting and Exhibit, 6-9 January 2003, Reno, Nevada, AIAA Paper 2003-1095.

Braun, R. D. and Spencer, D. A. (2006) Design of the ARES Mars Airplane and Mission Architecture, Journal of Spacecraft and Rockets, vol. 43, no. 5, pp. 1026–1034.

Bueno-Orovio, A., Castro, C., Palacios, F., and Zuazua, E. (2012) Continuous Adjoint Approach for the Spalart–Allmaras Model in Aerodynamic Optimization, AIAA Journal, vol. 50, no. 3, pp. 631–646.

Cakmakcioglu, S. C., Bas, O. and Kaynak, U. (2018) A Correlation-Based Algebraic Transition Model, Proc IMechE Part C: Journal of Mechanical Engineering Science, vol. 232(21), pp. 3915-3929.

Cohen, I. M., and Moraff, C. A. (1971). Viscous Inner Structure of Zero Prandtl Number Shocks, The Physics of Fluids, 14(6), 1279-1280.

Dhert, T., Ashuri, T. and Martins, J. R. R. A. (2017) Aerodynamic Shape Optimization of Wind Turbine Blades using a Reynolds-Averaged Navier-Stokes Model and an Adjoint Method, Wind Energy, vol. 20, pp. 909-926.

Drela, M. (1992) Transonic Low-Reynolds Number Airfoils, AIAA Journal of Aircraft, vol. 29, no. 6.

Driver, J. and Zingg, D. W. (2007) Numerical Aerodynamic Optimization Incorporating Laminar-Turbulent Transition Prediction, AIAA Journal, vol. 45, no. 8, pp. 1810-1818.

Economon, T. D., Palacios, F., Copeland, S. R., Lukaczyk, T. W. and Alonso, J. J. (2016) SU2: An Open-Source Suite for Multiphysics Simulation and Design, AIAA Journal, vol. 54, no. 3, pp. 828-846.

Greer, D., Hamory, P., Krake K. and Drela, M. (1999) Design and Predictions for a High-Altitude Low-Reynold Number Aerodynamic Flight Experiment, NASA TM-1999-206579, Dryden Flight Research Centre.

Halila, G. L. O., Chen, G., Shi, Y., Fidkowski, K.J. and Martins, J. R. R. A. (2019) High-Reynolds Number Transitional Flow Prediction using a Coupled Discontinuous-Galerkin RANS PSE Framework, AIAA SciTech Forum 2019, AIAA Paper 2019-0974.

He, X., Li, J., Mader, C.A., Yildirim, A. and Martins, J.R.R.A. (2019) Robust Aerodynamic Shape Optimization – From a Circle to an Airfoil, Aerospace Science and Technology, vol. 87, pp. 48-61.

Jameson, A., Schmidt, W., and Turkel, E. (1981) Numerical Solution of the Euler Equations by Finite Volume Methods Using Runge-Kutta Time Stepping Schemes, AIAA Paper 1981-1259.

Jung, J., Yee, K., Misaka, T. and Jeong, S. (2017) Low Reynolds Number Airfoil Design for a Mars Exploration Airplane Using a Transition Model, Transactions of the Japan Society for Aeronautical and Space Sciences, vol. 60, no. 6, pp. 333-340.

Kaynak, U., Cakmakcioglu, S. C. and Genc, M. S. (2012) Transition at Low-Re Numbers for some Airfoils at High Subsonic Mach Numbers, in Low Reynolds Number Aerodynamics and Transition, IntechOpen.

Kaynak, U., Bas, O., Cakmakcioglu, S. C. and Tuncer, I. H. (2019) Transition Modeling for Low to High Speed Boundary Layer Flows with CFD Applications, in Boundary Layer Flows-Theory, Applications and Numerical Methods, IntechOpen.

Khayatzadeh, P. and Nadarajah, S. K. (2011) Aerodynamic Shape Optimization via Discrete Viscous Adjoint Equations for the $k - \omega\, SST$ Turbulence and $\gamma - Re_\theta$ Transition Models, 49th AIAA Aerospace Sciences Meeting, 4-7 January 2011, Orlando, Florida, AIAA Paper 2011-1247.

Khayatzadeh, P. and Nadarajah, S. K. (2014) Laminar-Turbulent Flow Simulation for Wind Turbine Profiles Using the $\gamma - Re_\theta$ Transition Model, Wind Energy, vol. 17, pp. 901-918.

Kraft, D. (1988) A Software Package for Sequential Quadratic Programming, Technical Report DFVLR-FB 88-28, DLR German Aerospace Centre - Institute for Flight Mechanics, Koln.

Lee, J. D. and Jameson, A., (2009) NLF Airfoil and Wing Design by Adjoint Method and Automatic Transition Prediction, 27th AIAA Applied Aerodynamics Conference, 22-25 June 2009, San Antonio, Texas, AIAA Paper 2009-3514.

McGhee, R. J., Walker, B. S. and Millard, B. F. (1988) Experimental Results for the Eppler 387 Airfoil at Low Reynolds Numbers in the Langley Low-Turbulence Pressure Tunnel, NASA Technical Memorandum 4062, Langley Research Centre.

Menter, F. R., Langtry, R. B., Likki, S. R., Suzen, Y. B., Huang, P. G., and Völker, S. (2004) A Correlation-Based Transition Model Using Local Variables Part I: Model Formulation, Proceedings of ASME Turbo Expo 2004, pp. 57–67.

Munday, P. M., Taira, K., Suwa, T., Numata, D. and Asai, K. (2015) Nonlinear Lift on a Triangular Airfoil in Low-Reynolds-Number Compressible Flow, AIAA Journal of Aircraft, vol. 52, no. 3, pp. 924-931.

Puckett, A. E. and Stewart, H. J. (1950) The Thickness of a Shock Wave in Air, Quarterly of Applied Mathematics Vol. 7, No. 4, pp. 457-463.

Rashad, R. and Zingg, D. W. (2015) Aerodynamic Shape Optimization for Natural Laminar Flow using a Discrete-Adjoint Approach, 22nd AIAA Computational Fluid Dynamics Conference, 22-26 June 2015, Dallas, Texas, AIAA Paper 2015-3061.

Riedel, H. and Sitzmann, M. (1998) In-Flight Investigations of Atmospheric Turbulence, Aerospace Science and Technology, vol. 5, pp. 301-319.

Robitaille, M., Mosahebi, A. and Laurendeau, E. (2015) Design of Adaptive Transonic Laminar Airfoils Using the $\gamma - Re_{\theta}$ Transition Model, Aerospace Science and Technology, vol. 46, pp. 60-71.

Sederberg, T. W. and Parry, S. R. (1986) Free-form Deformation of Solid Geometric Models, SIGGRAPH Computer Graphics, vol. 20, no. 4, pp. 151–160.

Smith, S. C., Guynn, M. D., Streett, C. L. and Beeler, G. B. (2003) Mars Airplane Airfoil Design with Application to ARES, 2nd AIAA Unmanned Systems, Technologies and Operations Conference, 15-18 September 2003, San Diego, California, AIAA Paper 2003-6607.

Spalart, P. R. and Allmaras, S. R. (1992) A One-Equation Turbulence Model for Aerodynamic Flows, 30th Aerospace Sciences Meeting and Exhibit, 6-9 January 1992, Reno, Nevada, AIAA Paper 92-0439.

Tanaka, Y., Okabe, Y., Suzuki, H., Nakamura, K., Kubo, D., Tokuhiro, M. and Rinoie, K. (2006) Conceptual Design of Mars Airplane for Geographical Exploration, Journal of the Japan Society for Aeronautical and Space Sciences, vol. 54, no. 624, pp. 24–26.

Vassberg, J. C., Foch, R. J., Page, G. S. and Jameson, A. (2004) Aerodynamic Design and Optimization of the Mars ARES Aircraft, 42nd AIAA Aerospace Sciences Meeting and Exhibit, 5-8 January 2004, Reno, Nevada, AIAA Paper 2004-401.

Walters, D. K. and Leylek, J. H. (2004) A New Model for Boundary-Layer Transition Using a Single Point RANS Approach, ASME Journal of Turbomachinery, vol. 126, pp. 193-202.

Yang, G., Da Ronch, A., Drofelnik, J. and Xie, J.T. (2018) Sensitivity Assessment of Optimal Solution in Aerodynamic Design Optimisation Using SU2, Aerospace Science and Technology, vol. 81, pp. 362-374.

Young, L.A. (2000) Vertical Lift – Not Just for Terrestrial Flight, AHS/AIAA/RAeS/SAE International Powered Lift Conference, 30 October - 1 November 2000, Arlington, Virginia.

Zhang, S., Li, H. and Abbasi, A.A. (2019) Design Methodology Using Characteristic Parameters Control for Low Reynolds Number Airfoils, Aerospace Science and Technology, vol. 86, pp. 143-152.

Table 1. Properties of grids used for convergence study

Grid	No. Cells	Cells on Wall	Max y^+
Coarse	6400	80	1.33
Medium	25600	160	0.66
Fine	102400	320	0.33

Table 2. Summary of convergence study results

Fully Turbulent (SA)			
Grid	C_L	$C_D\ [cts]$	C_m
Coarse	0.61187	256.54	0.08750
Medium	0.63889	219.43	0.09007
Fine	0.64959	213.16	0.09169
Richardson Extrapolation	0.65660	211.88	0.09447
Order of Convergence	1.33631	2.56527	0.66207
Range of Convergence	1.01674	0.97142	1.01799
Grid Convergence Index	0.0135	0.0075	0.0279
Transitional (SA-BC)			
Grid	C_L	$C_D\ [cts]$	C_m
Coarse	0.54298	214.39	0.07822
Medium	0.66110	185.77	0.09447
Fine	0.66508	171.88	0.09664
Richardson Extrapolation	0.66522	158.78	0.09697
Order of Convergence	4.89097	1.04297	2.90946
Range of Convergence	1.00602	0.92523	1.02290
Grid Convergence Index	0.0002	0.0095	0.0042

Table 3. Results of multi-point and single-point optimization

`	**Mach Number**	**Multi-point** C_D $[cts]$	**Single-point** C_D $[cts]$	ΔC_D $[cts]$
Transitional	0.66	177.11	171.49	5.62
	0.68	202.30	191.20	11.10
	0.70	311.39	263.35	48.04
Turbulent	0.66	233.31	201.91	31.40
	0.68	237.73	209.66	28.07
	0.70	242.30	236.04	6.26

Table 4. Drag components breakdown for multi-point and single-point optimization

`	**Mach**	**Multi-point** C_{D_p} $[cts]$	**Single-point** C_{D_p} $[cts]$	ΔC_{D_p} $[cts]$	**Multi-point** C_{D_f} $[cts]$	**Single-point** C_{D_f} $[cts]$	ΔC_{D_f} $[cts]$
Transitional	0.66	112.33	109.34	2.99	64.78	62.15	2.63
	0.68	138.41	133.04	5.37	63.89	58.17	5.72
	0.70	254.60	206.76	47.84	56.79	56.60	0.19
Turbulent	0.66	113.91	94.24	19.67	119.40	107.66	11.74
	0.68	119.75	103.69	16.06	117.99	105.97	12.02
	0.70	125.90	132.89	-6.99	116.40	103.15	13.25

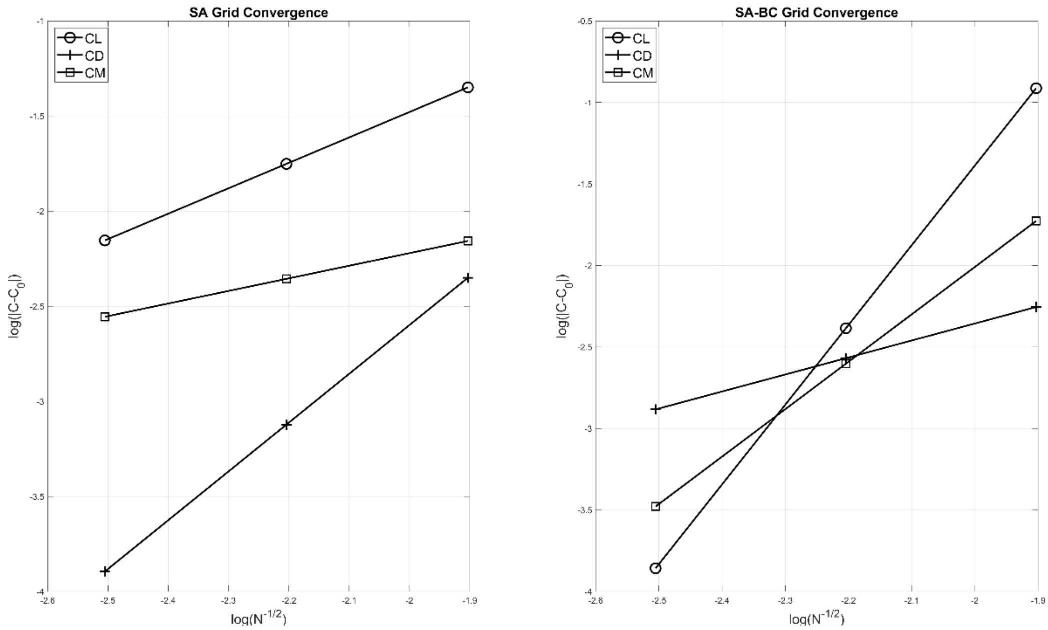

Figure 1. Grid convergence of aerodynamic coefficients

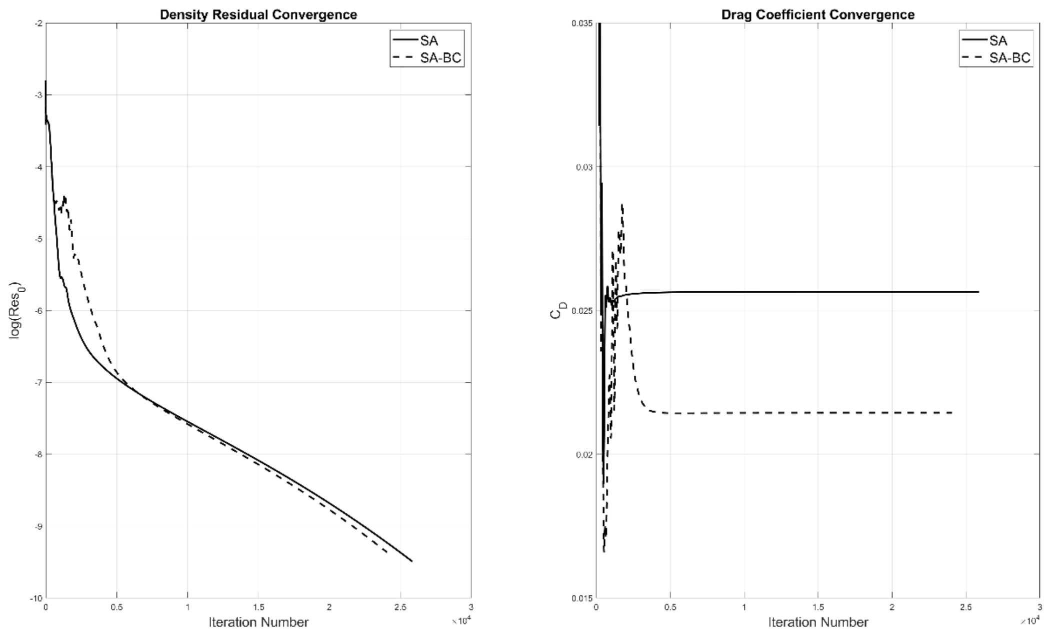

Figure 2. Convergence behaviour of density residual and drag coefficient

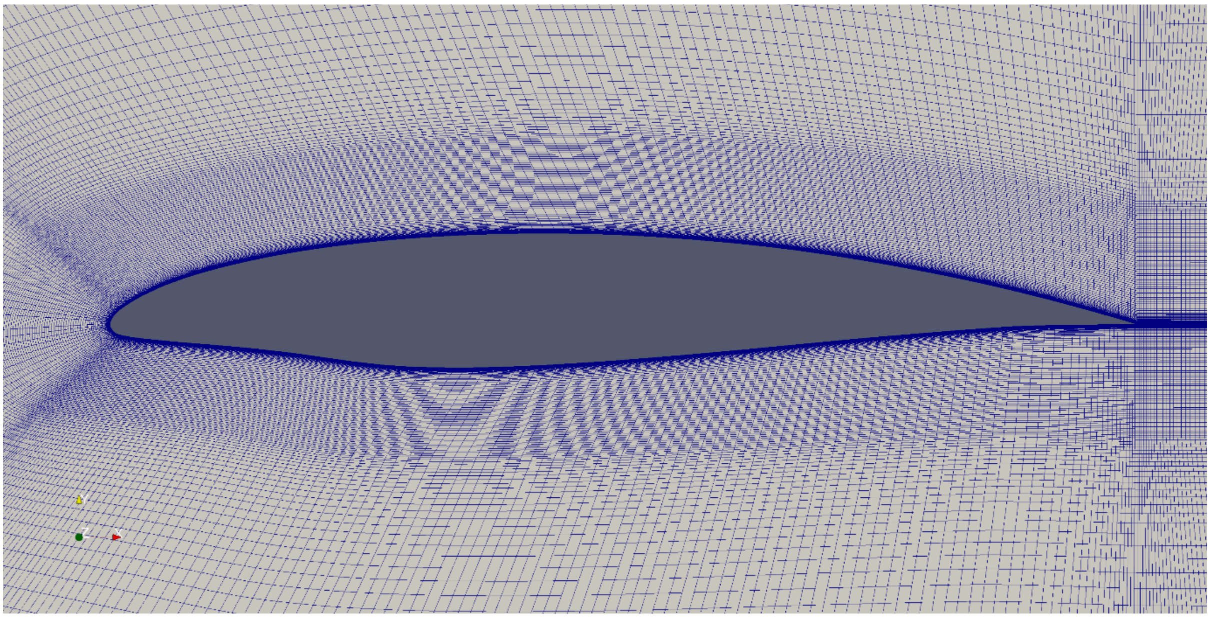

Figure 3. Close-up view of fine level grid around airfoil surface

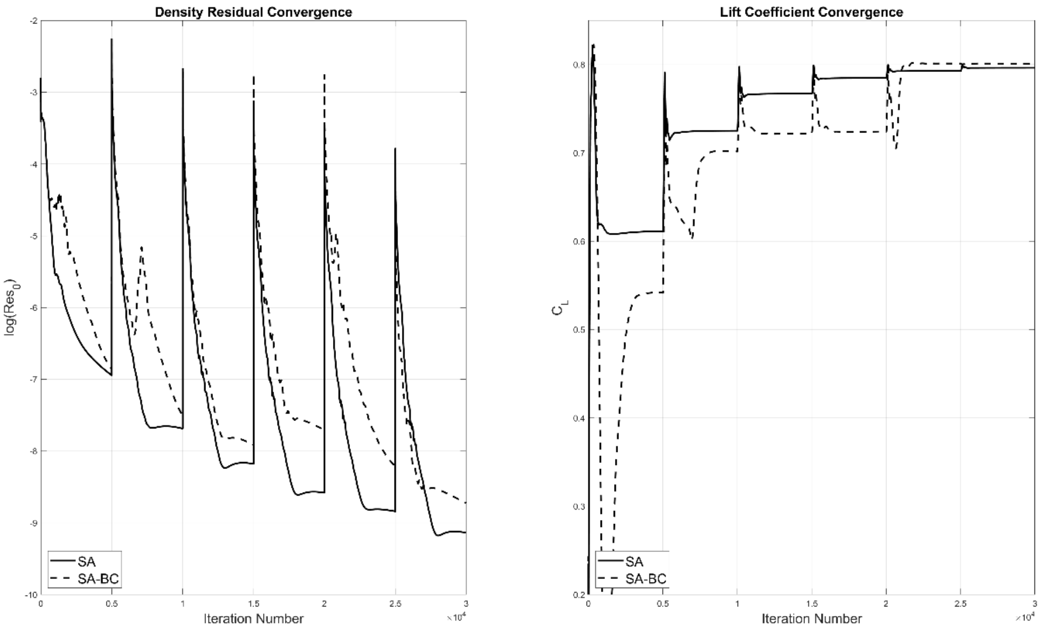

Figure 4. Convergence behaviour of density residual and lift coefficient when fixed C_L is required

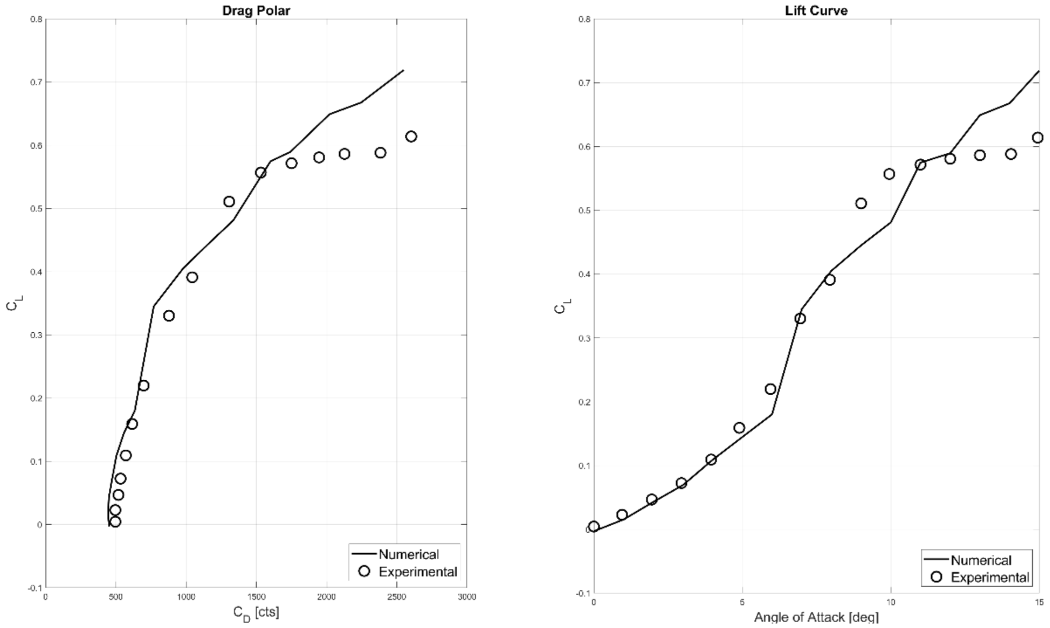

Figure 5. Verification of transition model for NACA 0012-34 airfoil at M = 0.61 and Reynolds number of 11000 in CO2

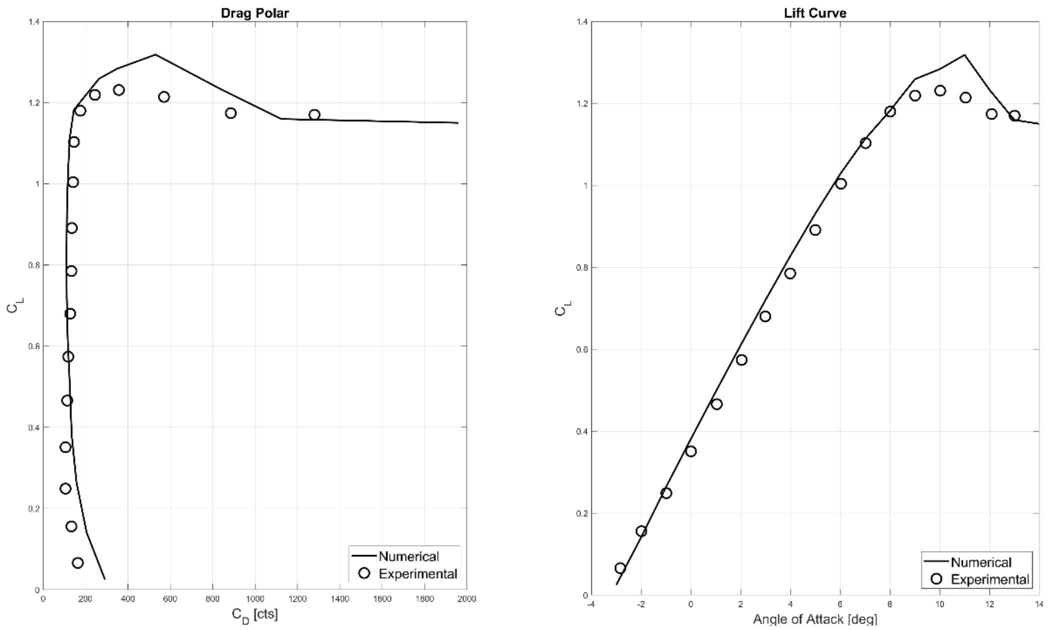

Figure 6. Verification of transition model for Eppler E387 airfoil at M = 0.06 and Reynolds number of 200000

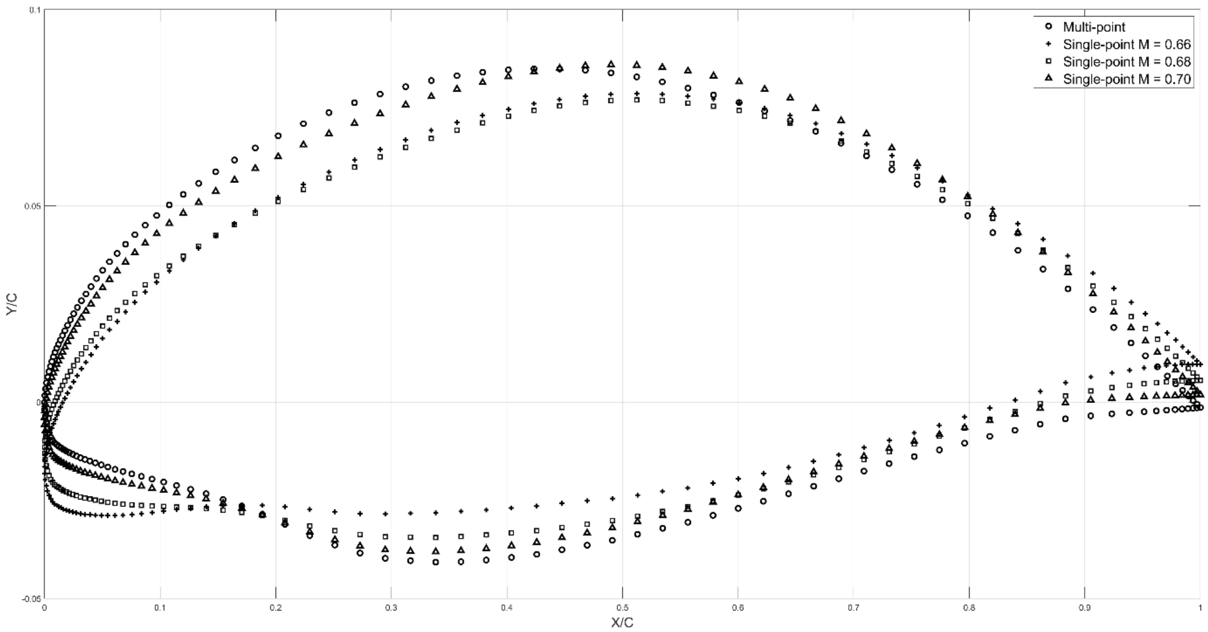

Figure 7. Contour of optimal airfoils obtained with transition model

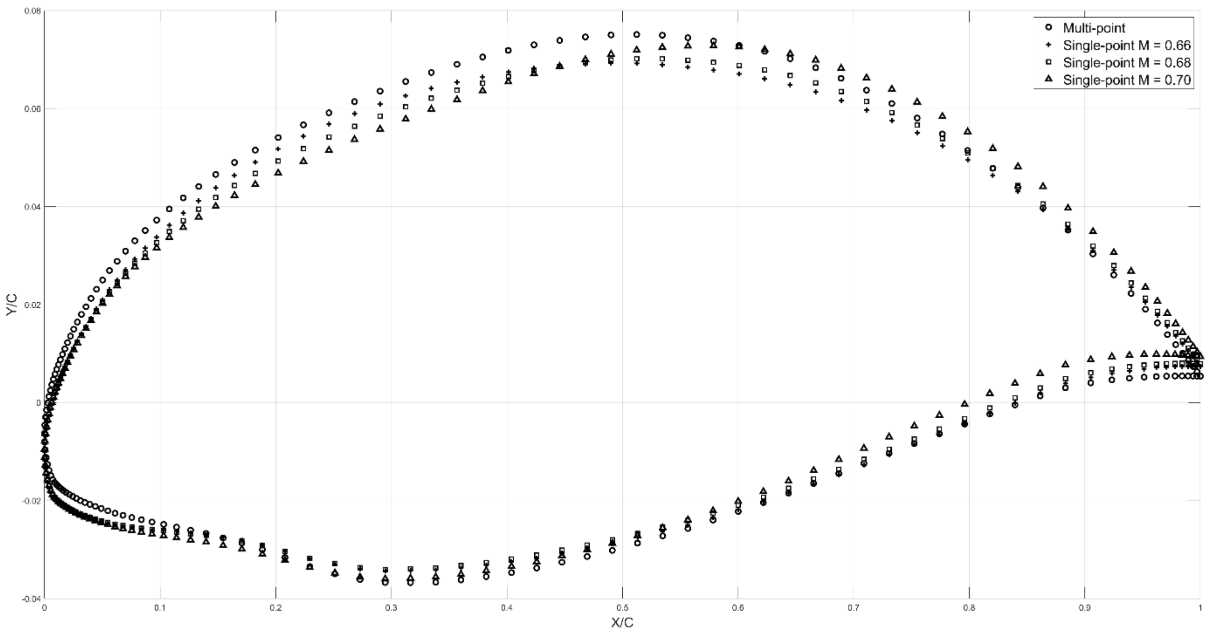

Figure 8. Contour of optimal airfoils obtained with fully turbulent model

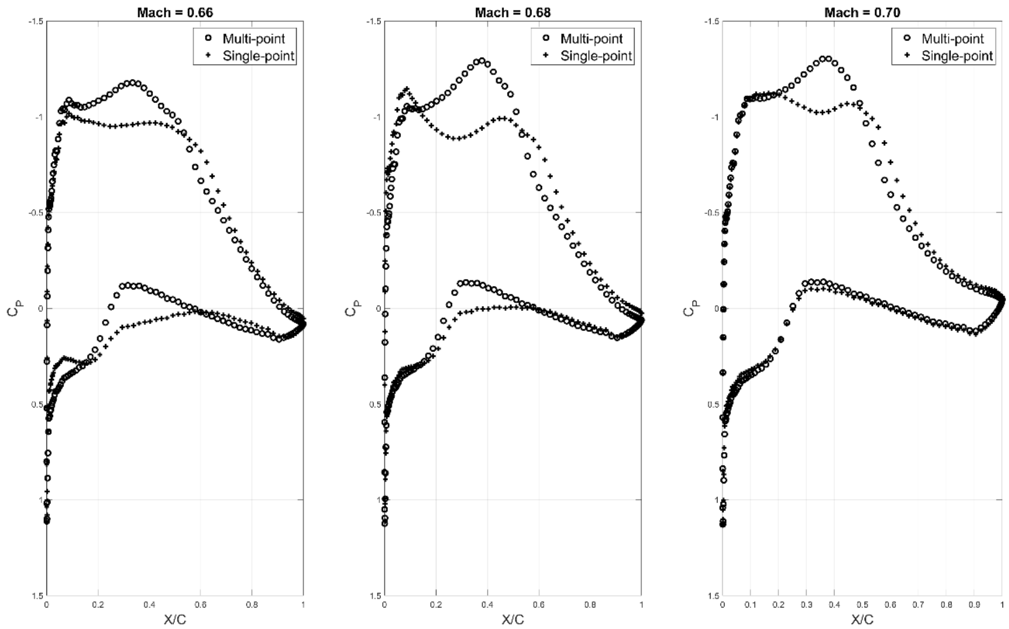

Figure 9. Pressure coefficient distribution of optimized airfoils for each Mach number, transitional case

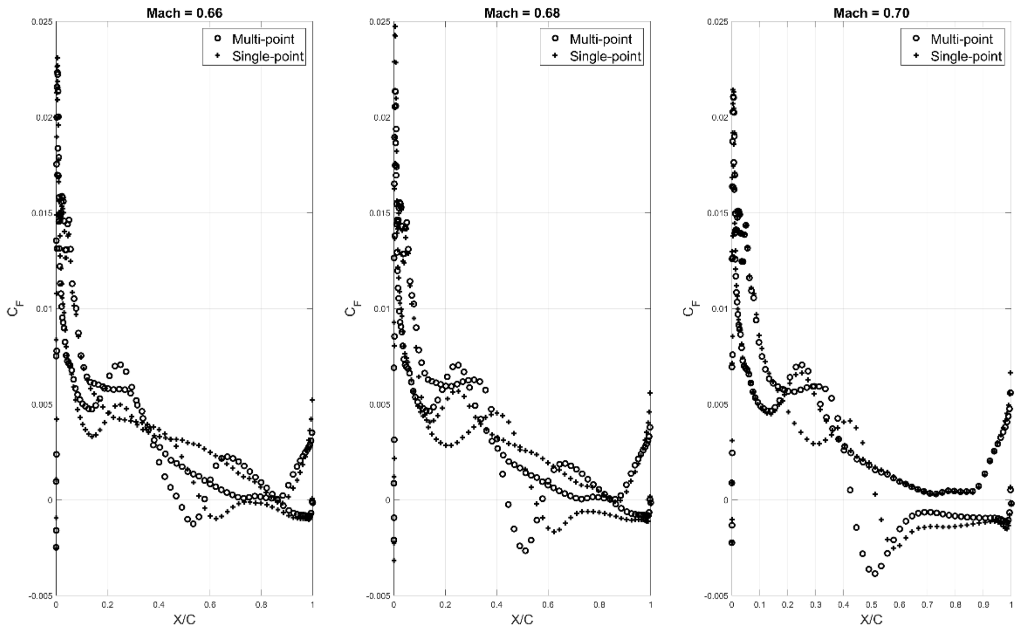

Figure 10. Skin friction coefficient distribution of optimized airfoils for each Mach number, transitional case

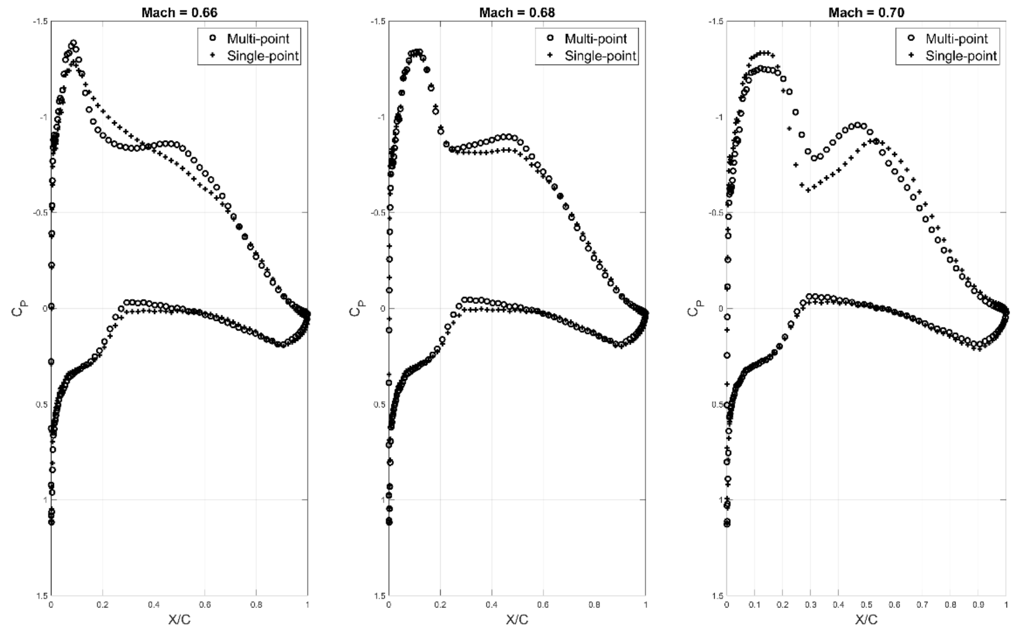

Figure 11. Pressure coefficient distribution of optimized airfoils for each Mach number, fully turbulent case

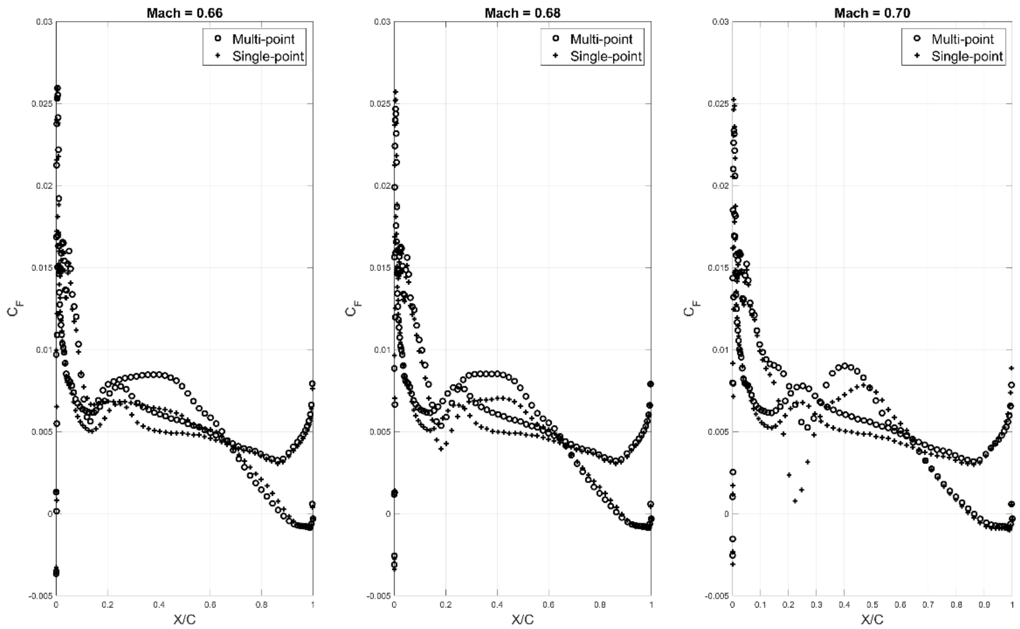

Figure 12. Skin friction coefficient distribution of optimized airfoils for each Mach number, fully turbulent case

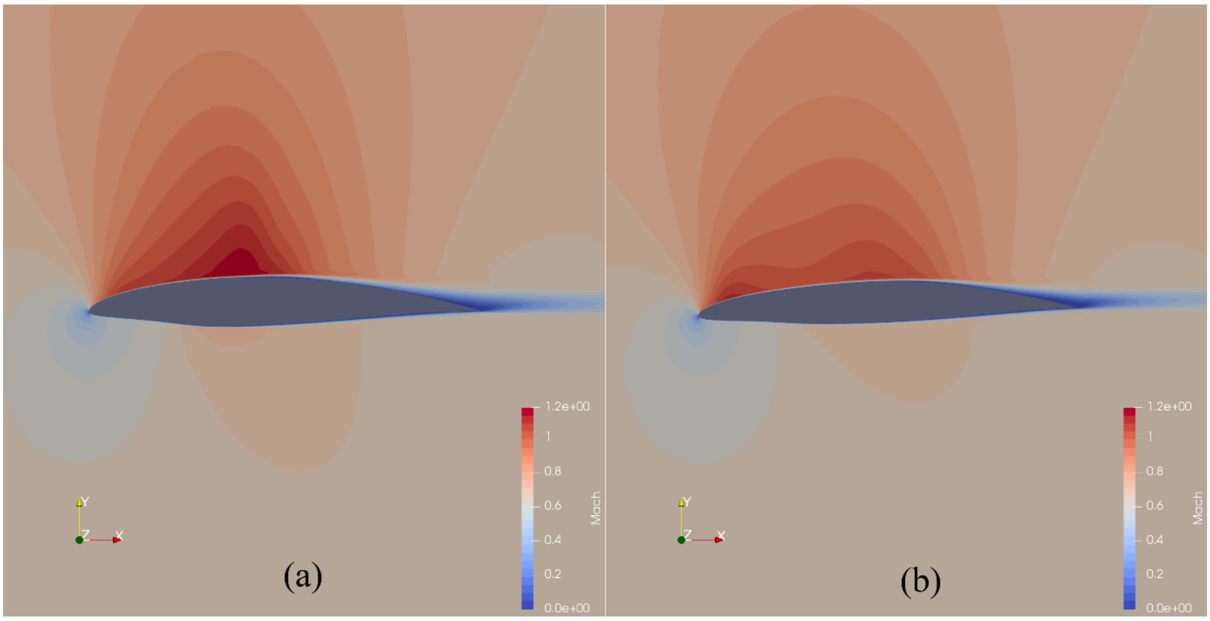

Figure 13. Comparison of Mach number contours around (a) the multi-point optimized airfoil for transitional flow at M = 0.68 and (b) the single-point optimized airfoil for transitional flow at M = 0.68

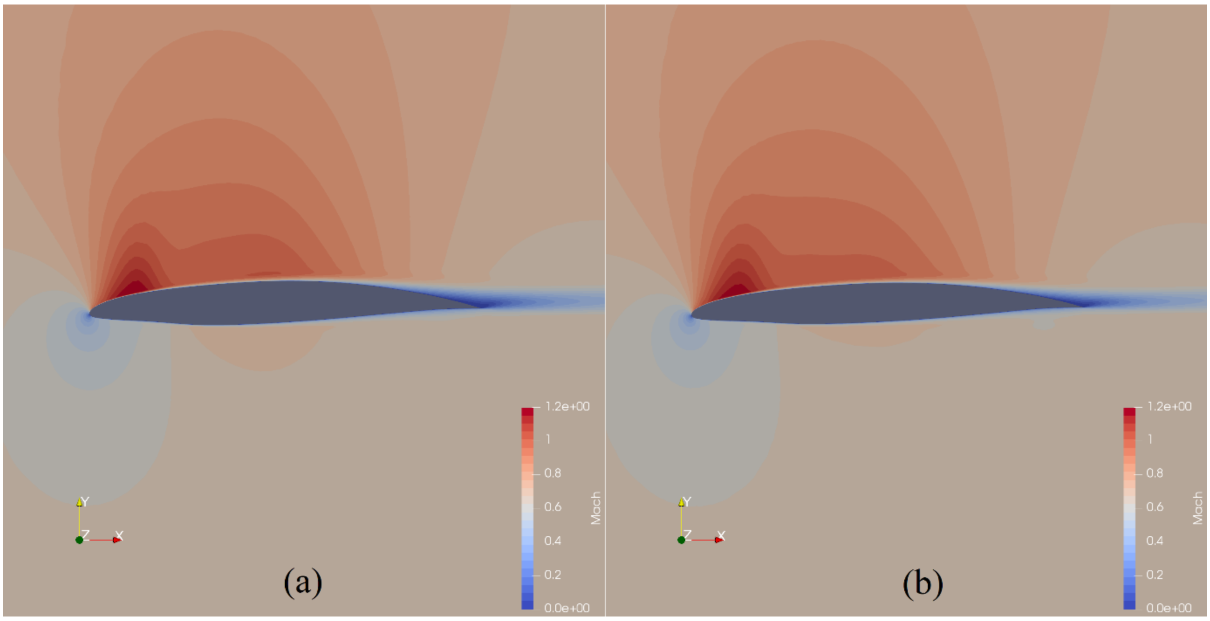

Figure 14. Comparison of Mach number contours around (a) the multi-point optimized airfoil for fully turbulent flow at M = 0.68 and (b) the single-point optimized airfoil for fully turbulent flow at M = 0.68

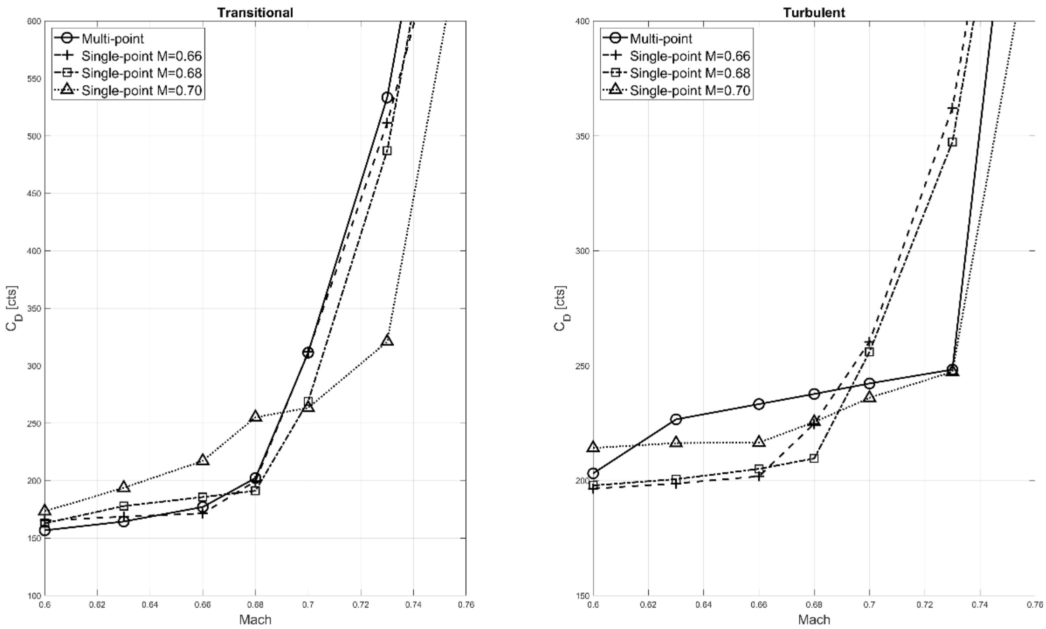

Figure 15. Drag rise curves for the multi-point and single-point optimized airfoils

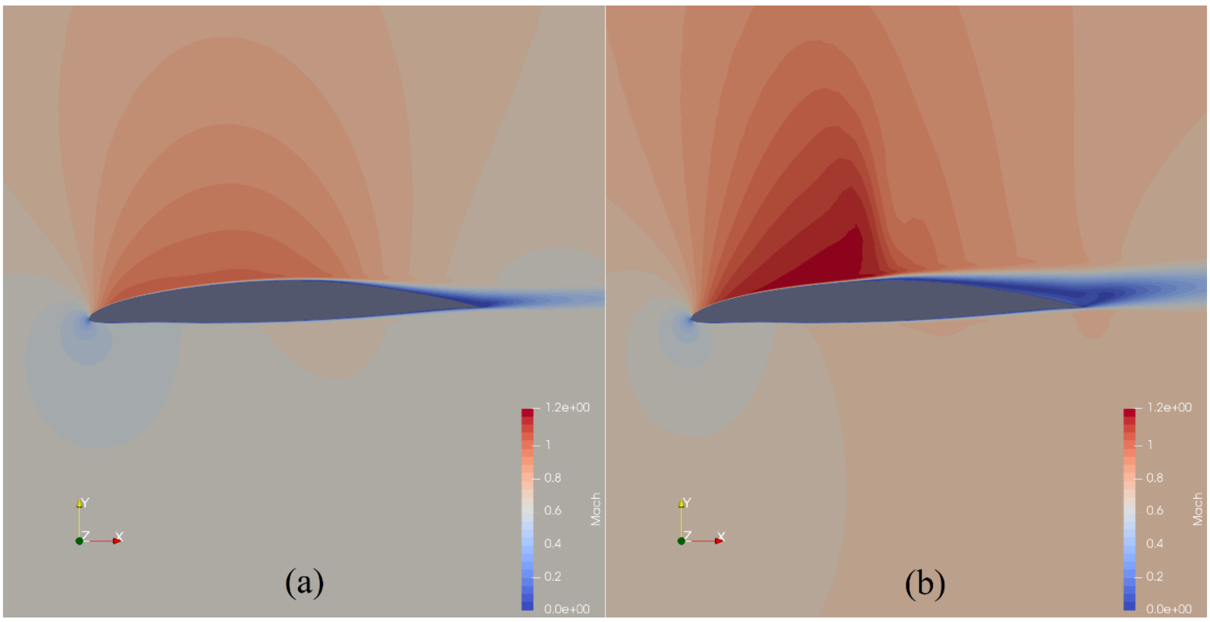

Figure 16. Comparison of Mach number contours around the transitional M = 0.66 single-point optimized airfoil when (a) operating on-design and (b) operating off-design at M = 0.73

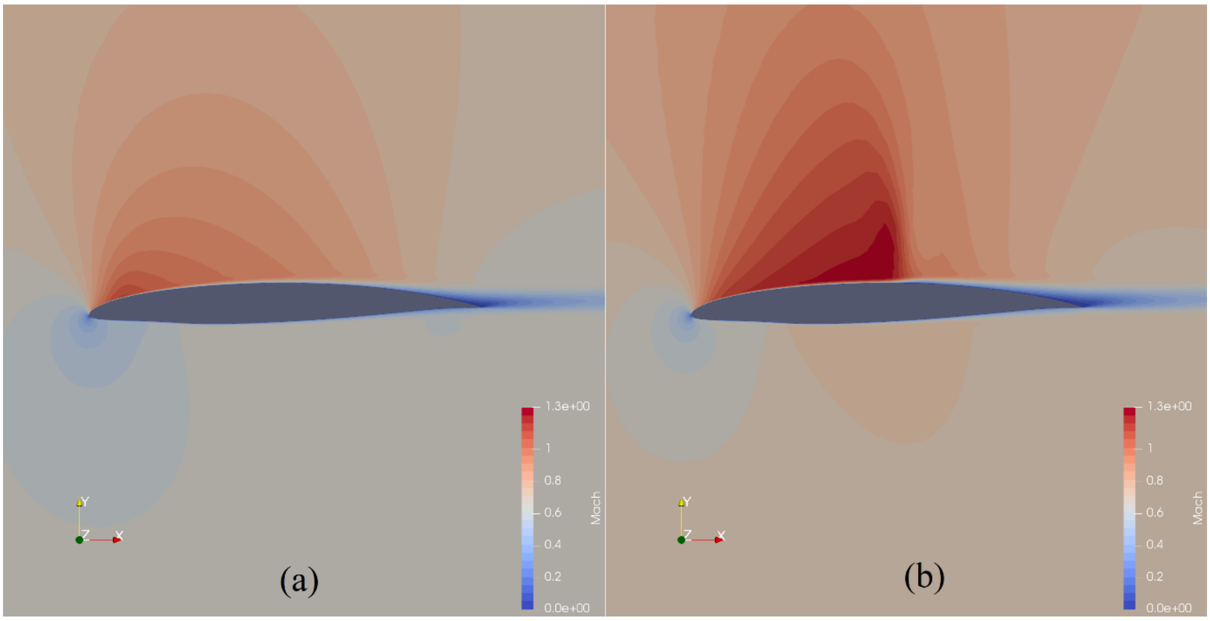

Figure 17. Comparison of Mach number contours around the fully turbulent M = 0.66 single-point optimized airfoil when (a) operating on-design and (b) operating off-design at M = 0.73

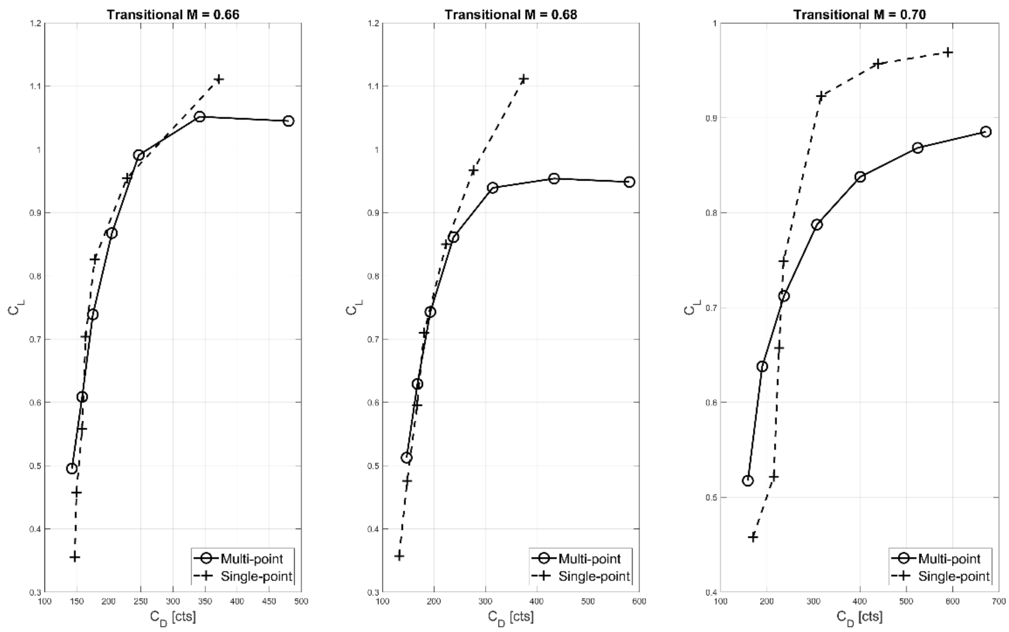

Figure 18. Drag polar for multi-point and single-point optimized airfoils, transitional flow

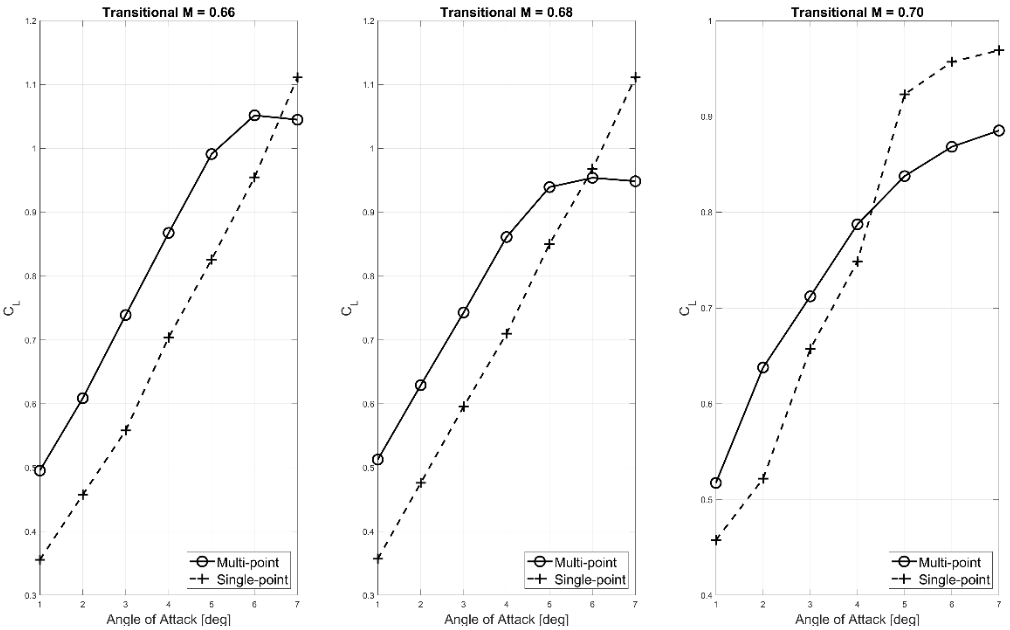

Figure 19. Lift curve for multi-point and single-point optimized airfoils, transitional flow

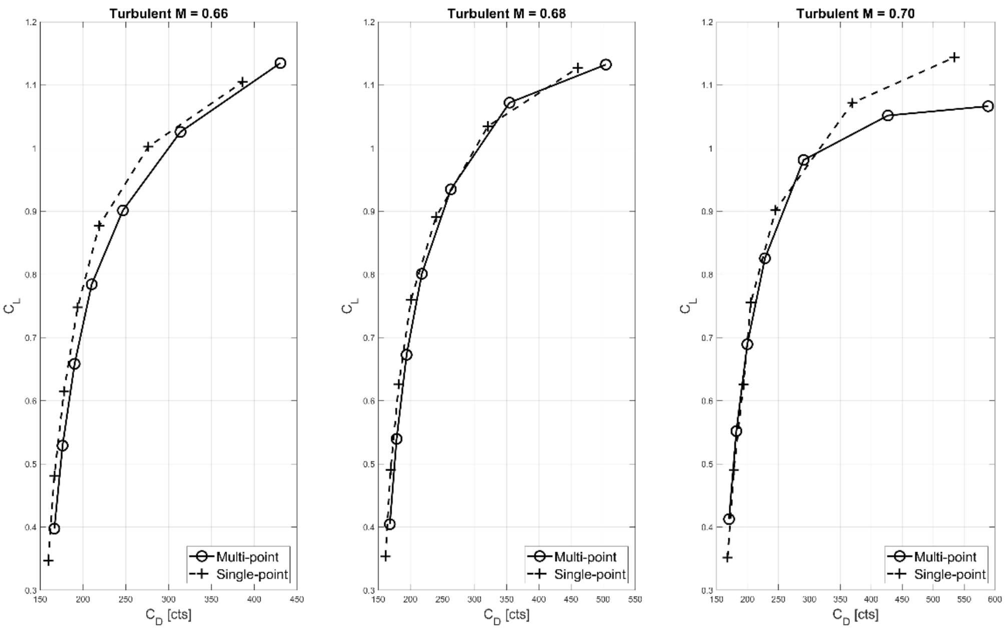

Figure 20. Drag polar for multi-point and single-point optimized airfoils, fully turbulent flow

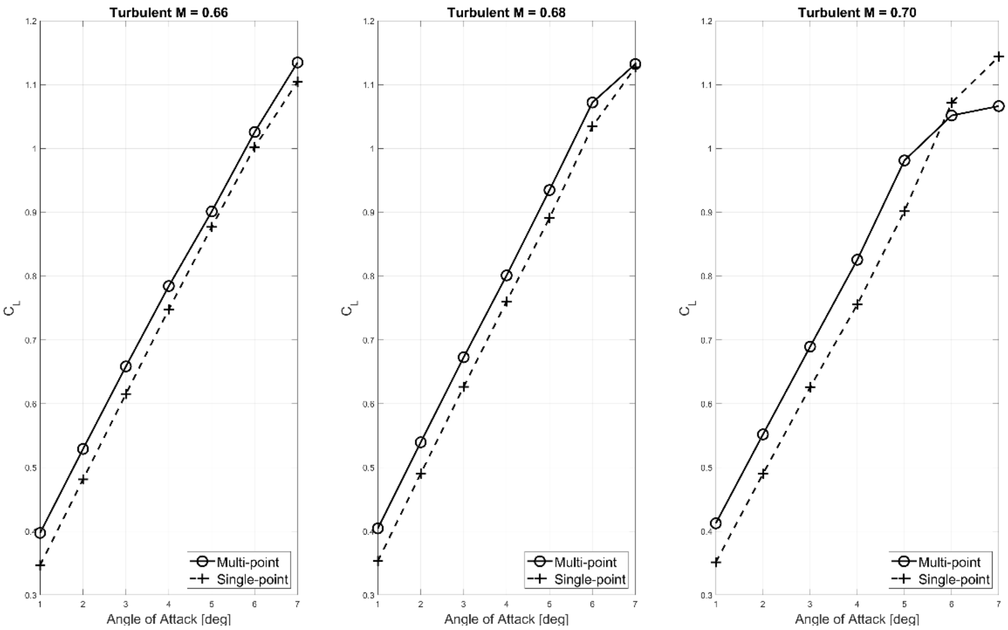

Figure 21. Lift curve for multi-point and single-point optimized airfoils, fully turbulent flow

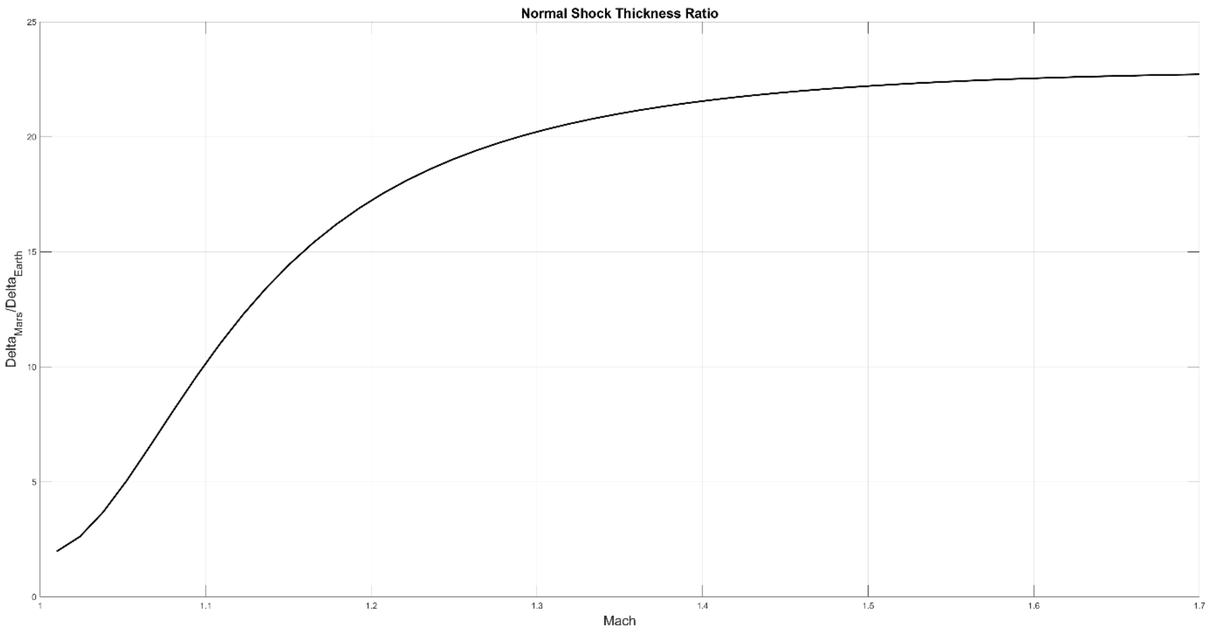

Figure A1. Ratio between normal shock wave thickness in low-altitude flight on Mars and flight at 11km altitude in Earth's atmosphere